Full Length Article

High-performance self-powered amorphous-BaTiO$_3$/p-Si heterojunction photodetector controlled by ferroelectric effect

Wushuang Han [a,b], Kewei Liu [a,b,*], Jialin Yang [a], Xing Chen [a,b], Qiu Ai [a], Yongxue Zhu [a], Zhen Cheng [a], Binghui Li [a], Lei Liu [a,b], Dezhen Shen [a,b,*]

[a] State Key Laboratory of Luminescence and Applications, Changchun Institute of Optics, Fine Mechanics and Physics, Chinese Academy of Sciences, Changchun 130033, PR China
[b] Center of Materials Science and Optoelectronics Engineering, University of Chinese Academy of Sciences, Beijing 100049, PR China

ARTICLE INFO

ABSTRACT

The coupling of ferroelectric and photoelectric effects provides a promising alternative for enhancing the performance of the photodetectors. Here, a high-performance self-powered UV–visible photodetector enhanced by the ferroelectric effect has been demonstrated on amorphous BaTiO$_3$/p-Si heterojunction. When the depolarization field in the ferroelectric BaTiO$_3$ layer is in the same direction as the built-in field at the heterojunction, the responsivities of the device at 0 V can be significantly improved to 14 mA/W, 27 mA/W, and 223 mA/W at 254 nm, 365 nm, and 600 nm, respectively, which is superior to any other reported BaTiO$_3$-based self-driven photodetectors. In addition, the device possesses a quick response speed with rising/fall times of 450 μs/460 μs at 254 nm and 80 μs/140 μs at 600 nm. Moreover, due to the defect-assistant recombination of photogenerated carriers at the amorphous BaTiO$_3$/p-Si interface and grain boundaries in amorphous BaTiO$_3$, the spike of transient photocurrent can be visualized under 254 nm illumination. This work presents a novel strategy for the design and research of high-performance self-powered photodetectors.

1. Introduction

The photodetector, being a semiconductor device that can convert photons into electrical signals, is widely used in industries, daily life, and the military [1–3]. Since the energy crisis is becoming a global issue, it is imperative to save energy [4]. Therefore, self-powered photodetectors that can operate without any external bias have valid application potential for future low-energy consumption optoelectronics [5,6]. Due to the presence of the built-in electronic field in a PN junction, Schottky junction, or heterojunction, the photogenerated carriers could be separated spontaneously, which can independently realize self-powered photodetection [7,8]. In addition, to further improve the detection performance of self-powered devices, some novel physical effects such as piezoelectric, ferroelectric, and pyroelectric have been introduced into such devices that can promote the separation of photogenerated carriers [9–17]. Therefore, the self-powered photodetectors based on piezoelectric, pyroelectric, and/or ferroelectric semiconductors are expected to accomplish the above purpose.

Barium titanate (BaTiO$_3$, abbreviated as BTO), as a typical *n*-type perovskite material, possesses good ferroelectric, piezoelectric, pyroelectric, and nonlinear optical properties [18–20]. Recently, some self-powered photodetectors based on BTO have been reported, which utilize the spontaneous polarization generated by ferroelectricity or/and pyroelectricity, and have made a series of important achievements [21,22]. Yang et al. have demonstrated various self-powered photodetectors on the sintered BTO ceramic slice, and the photovoltaic–pyroelectric–piezoelectric coupled effect has been systematically investigated [23]. Li et al. employed BTO single crystal to realize the self-powered UV detector, and an extremely fast response speed could be achieved with a rising/fall time of ~ 200 ps [24]. However, the reported BTO self-powered photodetectors were mostly based on the simple metal/BTO structure, and they usually exhibited low responsivity. These factors point out that there is a pressing need to promote the performance of BTO-based photodetectors.

According to the previous reports, combining BTO with other semiconductors to form heterojunction could enhance the separation and

---

migration of the photogenerated electron-hole pairs. This property has been widely used to improve the optoelectronic conversion efficiency in the field of photocatalysis [25–28]. Therefore, it is expected to realize a high-performance self-powered photodetector based on the BTO heterojunction structure. However, very little information can be gathered about the photoresponse performance of ferroelectric BTO heterojunctions. Here, a BTO/Si heterojunction self-powered ultraviolet (UV)-visible photodetector has been designed and fabricated. The p-type silicon is chosen for the heterojunction device due to the advances in integration and cost-effectiveness. Amorphous BTO is deposited directly on the silicon substrate to form BTO/Si heterojunction. Compared with crystalline BTO, the growth of amorphous BTO is not affected by the crystal lattice of the substrate. It is also easier to fabricate on a large scale, so it can be used for the preparation of self-driven heterojunction photodetectors. At 0 V bias, the enhanced responsivity of the heterojunction device can be identified with a high response speed. The effect of the depolarization field in BTO on the performance of amorphous-BTO/p-Si heterojunction photodetector has been systematically investigated in the work. The successful combination of amorphous ferroelectric materials and silicon enables the fabrication of low-cost, large-area, integrated ferroelectric&optoelectronic devices.

2. Experimental section

2.1. Preparation of heterojunction photodetector

2.1.1. Preparation of amorphous BTO film

The amorphous BTO thin film was prepared on a p-Si (1 1 1) substrate by utilizing radio frequency magnetron sputtering at 500 °C using a BTO ceramic target. Argon was selected as the working gas (20 sccm) with a sputtering pressure of 1.3 Pa, and the sputtering power was fixed at 60 W. To test the transmission spectrum, the amorphous BTO film was grown on c-Al$_2$O$_3$ under the same conditions.

2.1.2. Preparation of amorphous-BTO/p-Si device

After the growth of the amorphous BTO film on the Si substrate, the photodetectors were demonstrated by preparing an indium electrode on top of the amorphous BTO film and a silver paste electrode on the backside of the Si substrate.

2.2. Analysis instruments

The ferroelectric hysteresis (*P-E*) loop of BTO was measured at 2 Hz employing a ferroelectric test system (Multiferroic 100, Radiant Technologies). The ultraviolet photoelectron spectroscopy (UPS) and the X-ray photoelectron spectroscopy (XPS) of the BTO film was characterized by a Thermo Sciencific Escalab 250Xi and a Thermo ESCALAB 250 spectrometer (the software used in the analysis was the XPSPEAK41), respectively. The crystal structure of the BTO film was characterized using solid X-ray diffraction (XRD) (Bruker D8GADDS, Cu Kα radiation, $\lambda = 0.1541$ nm). Atomic force microscopy (AFM) (Multimode-8, Bruck Instruments, Germany) estimated the BTO film surface roughness (the software used in the analysis was the NanoScope Analysis). Scanning electron microscope (SEM) (HITACHI S-4800, the mode of measurement: secondary electrons) evaluated the surface morphology and cross-sectional of the film. Optical properties were characterized by a UV-3101PC scanning spectrophotometer techniques.

2.3. Photoelectric measurements

The current–voltage (*I-V*) curves and photoresponse characteristics were tested by an Agilent B1500A semiconductor device analyzer. The oscilloscope (Tektronix DPO5104 digital oscilloscope) recorded the transient photoresponse characteristics.

3. Results and discussion

The surface and cross-sectional SEM images of BTO films on the p-Si substrate are presented in Fig. 1a. It can be seen that the surfaces of BTO films are very uniform and smooth with ~ 210 nm in thickness. Fig. 1b demonstrates the AFM image of the BTO surface, and the root-mean-square (RMS) surface roughness is only 0.554 nm in a scan size of 5 × 5 μm^2. Fig. 1c depicts the XRD pattern of the BTO film on the Si substrate. The absence of any peak other than the (1 1 1) diffraction peak of Si at around 28.4° indicates that the BTO film is amorphous. Fig. 1d represents the transmission spectrum of the amorphous BTO film on a sapphire substrate. The amorphous BTO film exhibits relatively high transparency of over 90 % in the visible region and a sharp transmission edge at around 280 nm. According to the Tauc plot (inset in Fig. 1d) obtained from the absorption spectrum (Fig. S1), the band gap of the amorphous BTO film is about 4.39 eV, which is comparable to that of the reported amorphous BTO (4.2–4.6 eV) [29]. The band bap of amorphous films is higher than that of the crystalline films and bulk single crystals (~3.2 eV). This observation can be explained by the increase in distance between atoms and disorder of the amorphous materials [30,31]. Fig. 1e is UPS spectrum of the amorphous BTO film, which was calibrated vs the Fermi edge of testing stage. Using the linear extrapolation method, the secondary electron cut-off energy ($E_{cut-off}$) and the distance between the Fermi level (E_{Fermi}) and the valance band minimum (VBM) are estimated to be 19.63 eV and 4.1 eV, respectively. And the work function (W_F) can be calculated to be 1.59 eV by $W_F=h\upsilon-E_{cut-off}$, where $h\upsilon$ is photon energy (21.22 eV).

Fig. 2a is the XPS wide-scan spectrum of amorphous BTO film over a range of 0–1200 eV. Obvious signals corresponding to Ti, Ba, and O in the film further reveal the growth of BTO on Si. Fig. 2b-d shows the XPS fine spectra of Ba, Ti, and O in the amorphous BTO film. In Fig. 2b, the Ba 3d spectrum consists of two peaks located at 779.75 (Ba 3d$_{5/2}$) and 794.95 eV (Ba 3d$_{3/2}$) from the Ba^{2+} oxide state [32]. In addition, the Ti 2p spectrum possesses two peaks located at 458.1 and 463.7 eV, corresponding to Ti 2p$_{3/2}$ and Ti 2p$_{1/2}$ of Ti^{4+} in BTO, respectively (Fig. 2c). No obvious signal for Ti^{3+} can be found in the Ti 2p XPS spectrum [33]. Fig. 2d gives the XPS spectrum of the O 1 s, which can be divided into two peaks by Gaussian fitting. The stronger peak O$_I$ at 529.6 eV originates from lattice oxygen of Ti-O bonds and the peak O$_{II}$ located at 531.4 eV can be attributed to the oxygen vacancies [33,34].

Fig. 3a depicts the schematic structure of the amorphous-BTO/p-Si photodetector. An indium electrode and a silver paste electrode were fabricated, respectively, on the top of the amorphous BTO film and at the back of the Si substrate. The size of the device is around 5 mm^2. Fig. 3b shows the polarization versus electric field (*P-E*) hysteresis loop of the amorphous BTO at room temperature and 2 Hz frequency, and the photograph of the ferroelectric test system is provided in Fig. S2. The *P-E* hysteresis loop suggests that the amorphous BTO film is ferroelectric with a weak remnant polarization due to its amorphous nature [35,36]. The unpolarized (unpoled) state of the device was attained by heating for 5 min the as-grown amorphous BTO film at 150 °C (the Curie point of BTO is ~ 120 °C). Additionally, to achieve the polarization, both positive and negative bias voltages (±30 V) were applied to the heterojunction for 50 s at room temperature. Herein, we define the polarization state generated by the application of a positive bias as the poling-up state and that of a negative bias as the poling-down state (see Fig. 3c-d). The *I-V* curve of the amorphous-BTO/p-Si heterojunction in unpoled state is shown in Fig. 3e with an obvious rectifying behavior. The linear *I-V* curves of In electrode on the amorphous BTO layer and the Ag electrode on the p-Si indicate the existence of Ohmic contacts at both electrodes (see Fig. S3). Therefore, the rectifying behavior must have come from the amorphous-BTO/p-Si heterojunction, and the difference of the *I-V* curves in different states (inset in Fig. 3e) should be associated with the superposition of the polarization field, the built-in electric field and the applied electric field.

The time-dependent photoresponse characteristics (*I-t* curves) of the
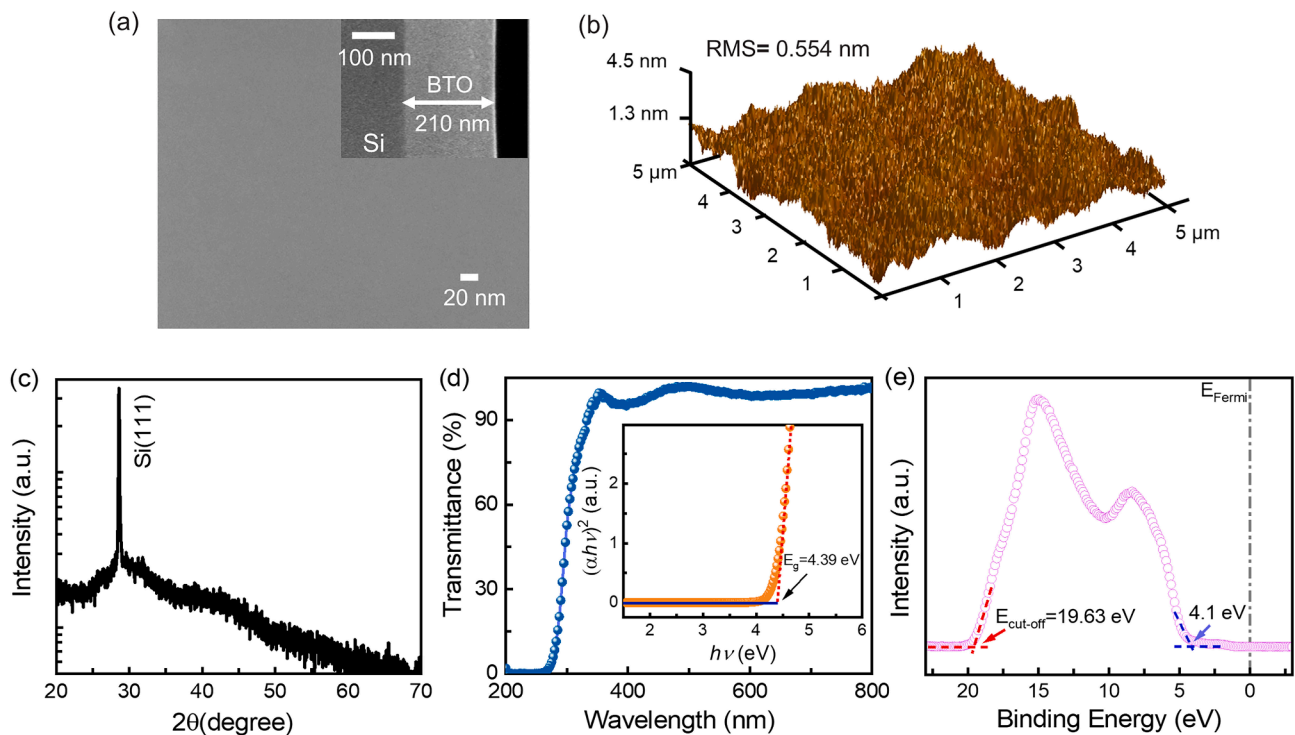
Fig. 1. (a) Surface morphology and cross-sectional SEM images of the amorphous BTO film. (b) The AFM image of the BTO surface. (c) XRD pattern of amorphous BTO film on the p-Si substrate. (d) The transmission spectrum and the Tauc plot of the amorphous BTO film deposited on sapphire. (e) UPS spectrum of the amorphous BTO film obtained at excitation photon energy ~ 21.22 eV.
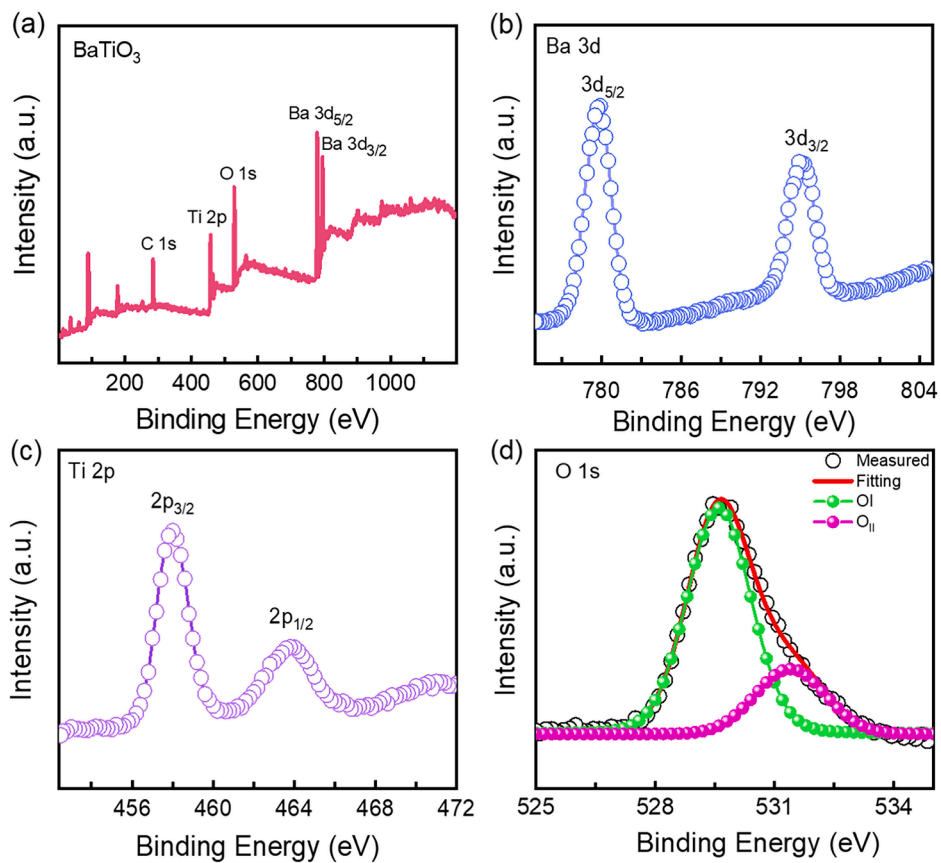

Fig. 2. (a) XPS survey spectrum of the amorphous BTO film. High resolution XPS spectra for (b) Ba 3d, (c) Ti 2p and (d) O 1 s.
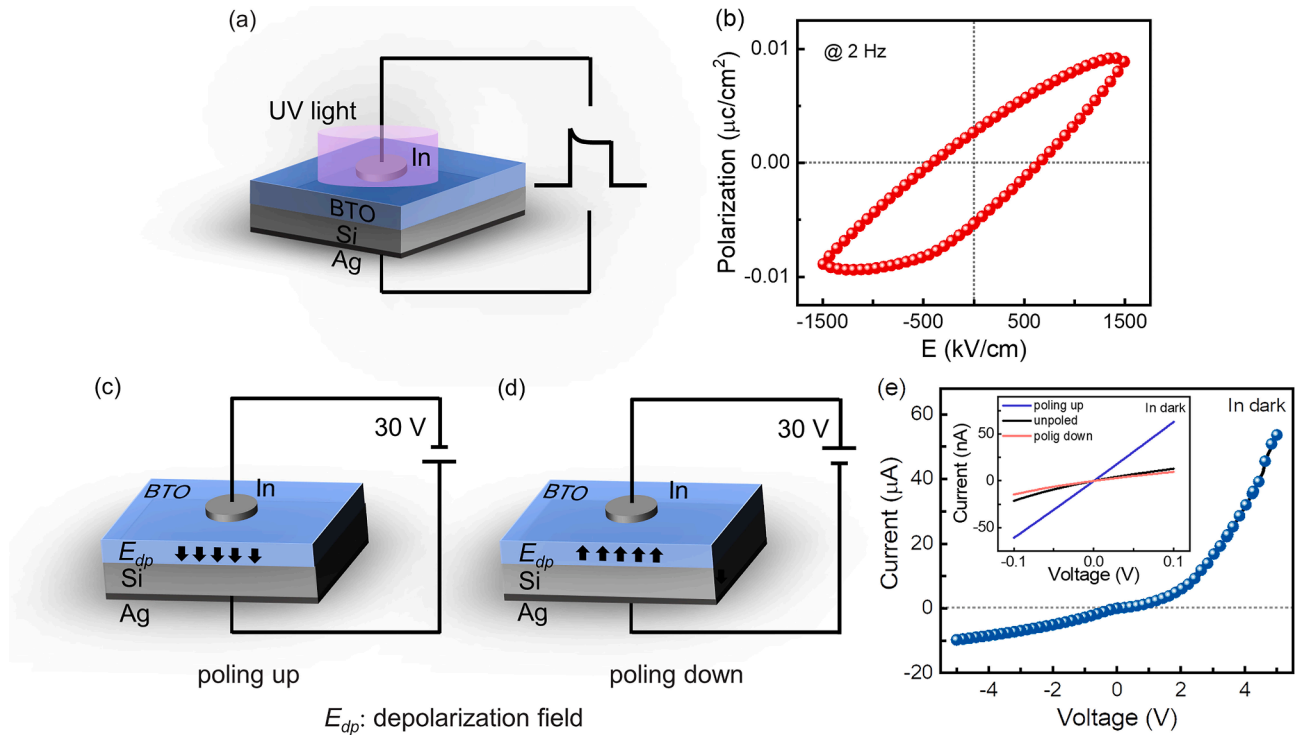
Fig. 3. (a) The schematic illustration of amorphous-BTO/p-Si photodetector under UV light. (b) The *P-E* loop of BTO measured at 2 Hz. The amorphous-BTO/p-Si heterojunction under (c) poling-up state and (d) poling-down state. (e) The *I-V* curves of the amorphous-BTO/p-Si heterojunction in dark.
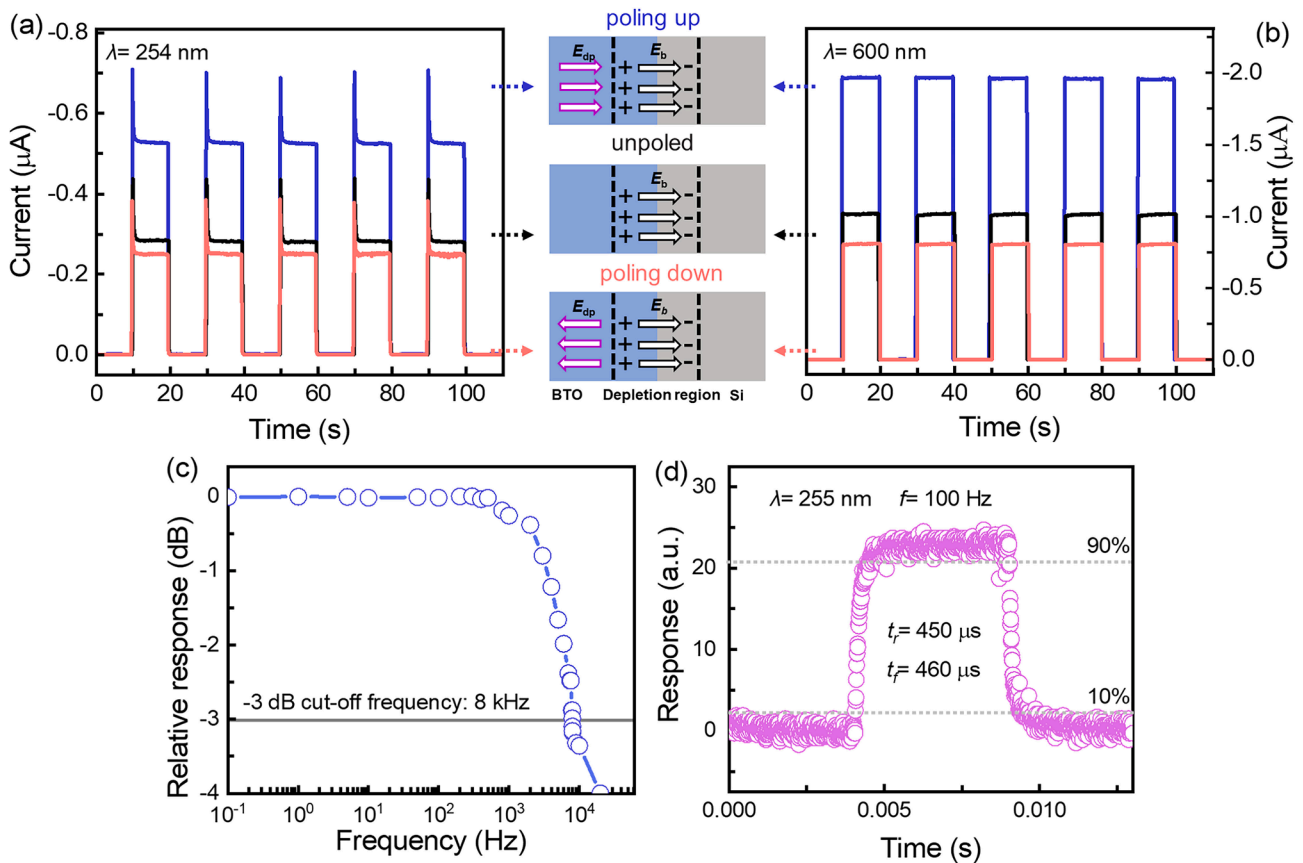

Fig. 4. Photocurrent responses of the amorphous-BTO/p-Si device at 0 V bias under various polarization states at (a) 254 nm and (b) 600 nm light illumination. (c) The frequency-dependent photoresponse of the amorphous-BTO/p-Si device. (d) One photoresponse cycle for estimating the rising time and the fall time at 100 Hz.

amorphous-BTO/p-Si photodetector were measured under 254 and 600 nm illuminations at 0 V (see Fig. 4a-4b), and the 365 nm illumination at 0 V is visualized in Fig. S4. Clearly, the device shows a quick, stable, and reproducible photoresponse to intermittent illumination. Moreover, in Fig. 4a, each photocurrent response consists of two stages under 254 nm illumination: a sharp peak (referred to as I_{peak}) and a stable current plateau (referred to as $I_{plateau}$). However, when irradiated under 600 nm light, only a steady current plateau can be observed. Notably, the photoresponse characteristics of the device can be adjusted by tuning the polarization direction. As shown in Fig. 4a and 4b, the built-in electric field (E_b) of the amorphous-BTO/p-Si heterojunction points to p-Si, so when the device is in the poling-up state, the built-in electric field is in the same direction as the ferroelectric polarization field (E_{dp}), increasing the photocurrent. In contrast, when the device is in the poling-down state, the built-in electric field is opposite to the ferroelectric polarization field, and the photocurrent decreases significantly. In addition, the response speed of the amorphous-BTO/p-Si photodetector was investigated by measuring the −3 dB cutoff frequency of the photoresponse as shown in Fig. 4c. The −3 dB cut-off frequency (frequency at the photoresponse reduces to 70.7 %) is calculated to be ~ 8 kHz at 254 nm and ~85.4 kHz at 600 nm (Fig. S6), suggesting that the amorphous-BTO/p-Si photodetector has a very fast response speed. Fig. S5 shows the transient photoresponse under 254 nm illumination at different frequencies. From one amplified response cycle at 100 Hz (Fig. 4d and S6), the rising/fall times (t_r/t_f) were calculated to be 450 μs/460 μs at 254 nm, 60 μs/140 μs at 365 nm and 80 μs/140 μs at 600 nm.

The responsivity R is an important parameter to evaluate the performance of the photodetector, which could be determined using the equation $R = I_{photo}$-$I_{dark}/S \bullet P_{inc}$, where I_{photo} is the steady photocurrent, I_{dark} is the dark current, S is the effective area of the device, and P_{inc} is the incident light power density. At the poling-up state, the responsivities of the device under 254 nm ($P_{254} = 1$ mW/cm^2), 365 nm ($P_{365} = 0.9$ mW/cm^2), and 600 nm ($P_{600} = 200$ μW/cm^2) light illuminations were calculated to be 14, 27, and 223 mA/W, respectively. In addition, the specific detectivity D* of the device at the poling-up state can be

evaluated to be 5.6×10^{11} (254 nm), 1.08×10^{12} (365 nm) and 8.92×10^{12} (600 nm) Jones by $D^*=R/\sqrt{(2qI_{dark}/S)}$, where q is the electronic charge.

Fig. 5a and 5b show the I-t curves of the amorphous-BTO/p-Si photodetector at different temperatures under 254 and 600 nm light illuminations, respectively. Upon increasing the temperature from 24 to 150 °C, the photocurrent of the device shows an obvious decrease in both the polarized and unpoled states. Below 120 °C (Curie point of BTO) [37], the photocurrent response of the device strongly depends on the polarization. But when the temperature exceeds 120 °C, the device gradually undergoes a transition from a polarized state to an unpoled state, so that the photocurrents in different states basically the same. After cooling down from 150 to 24 °C, the device is completely transformed into an unpoled state. The relative peak-to-plateau output current (I_{peak}-$I_{plateau}$) and $I_{plateau}$ extracted from Fig. 5a (254 nm) and Fig. 5b (600 nm) are plotted as a function of temperature in Fig. 5c-5e. It can be seen that upon increasing temperature, the device in the poling-up, unpoled or poling-down state exhibits a similar decreasing trend of $I_{plateau}$ under 254 nm and 600 nm illuminations (Fig. 5d and 5e). At temperatures above 120 °C, the device in polarized and unpoled states have nearly identical $I_{plateau}$ under 254 nm or 600 nm illumination. This phenomenon can be explained as the gradual weakening of the ferroelectric polarization with the increase of temperature and its complete disappearance above the Curie point. Fig. 5c presents the temperature-dependent relative peak-to-plateau output current (I_{peak}-$I_{plateau}$) under 254 nm illumination. When the temperature exceeds 120 °C, the device has almost the same I_{peak}-$I_{plateau}$ in the three different states.

Fig. 6a shows the energy band diagram of the equilibrium state of amorphous-BTO/p-Si heterojunction device in dark. The band gap and work function of p-Si were assumed to be 1.12 eV and ~4.7 eV, respectively. Since the transient spike phenomenon can be observed when the incident light wavelength is 254 nm (Fig. 4a), but not at 600 nm (Fig. 4b), it should be associated with the amorphous BTO layer according to the bandgap energies of amorphous BTO and p-Si. Taking the device in the poling-up state as an example, the mechanism of the
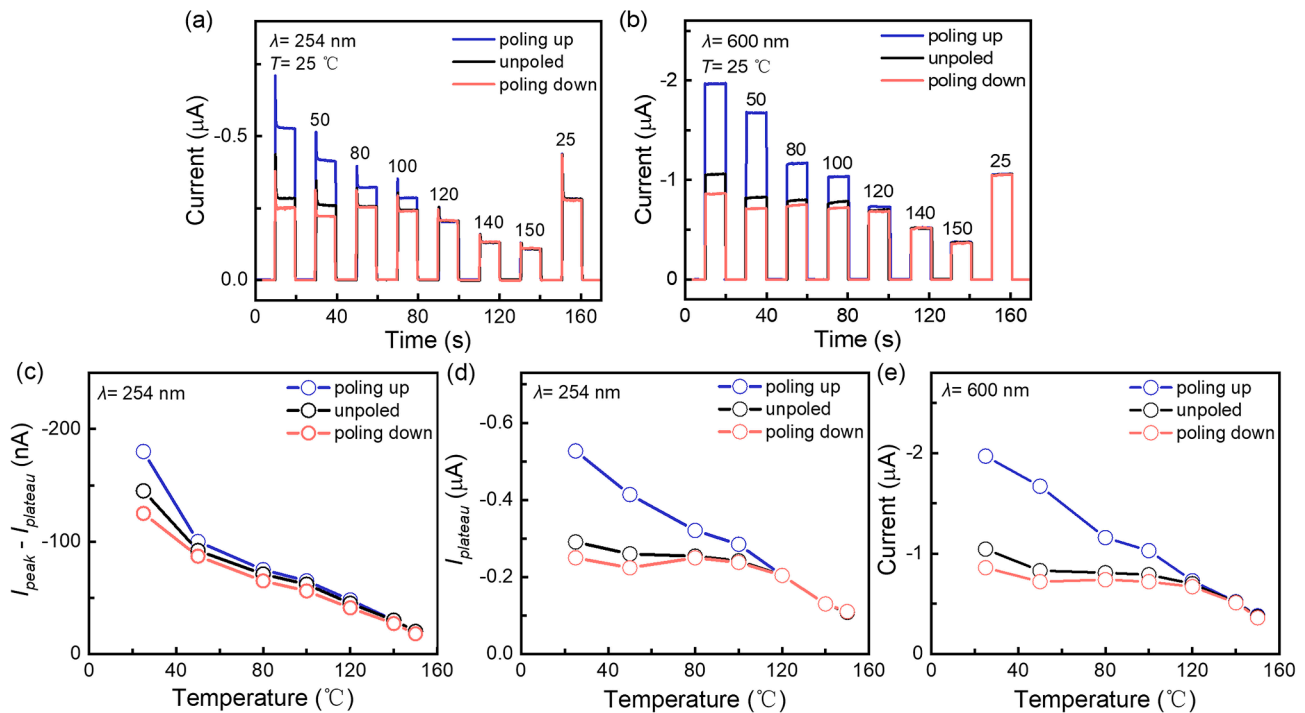

Fig. 5. Photocurrent responses of the amorphous-BTO/p-Si device at 0 V bias at various polarization states and various temperatures under (a) 254 nm and (b) 600 nm light illumination. The relative peak-to-plateau output current (c) and the $I_{plateau}$ under the (d) 254 nm and (e) 600 nm light illuminations as a function of the temperature.
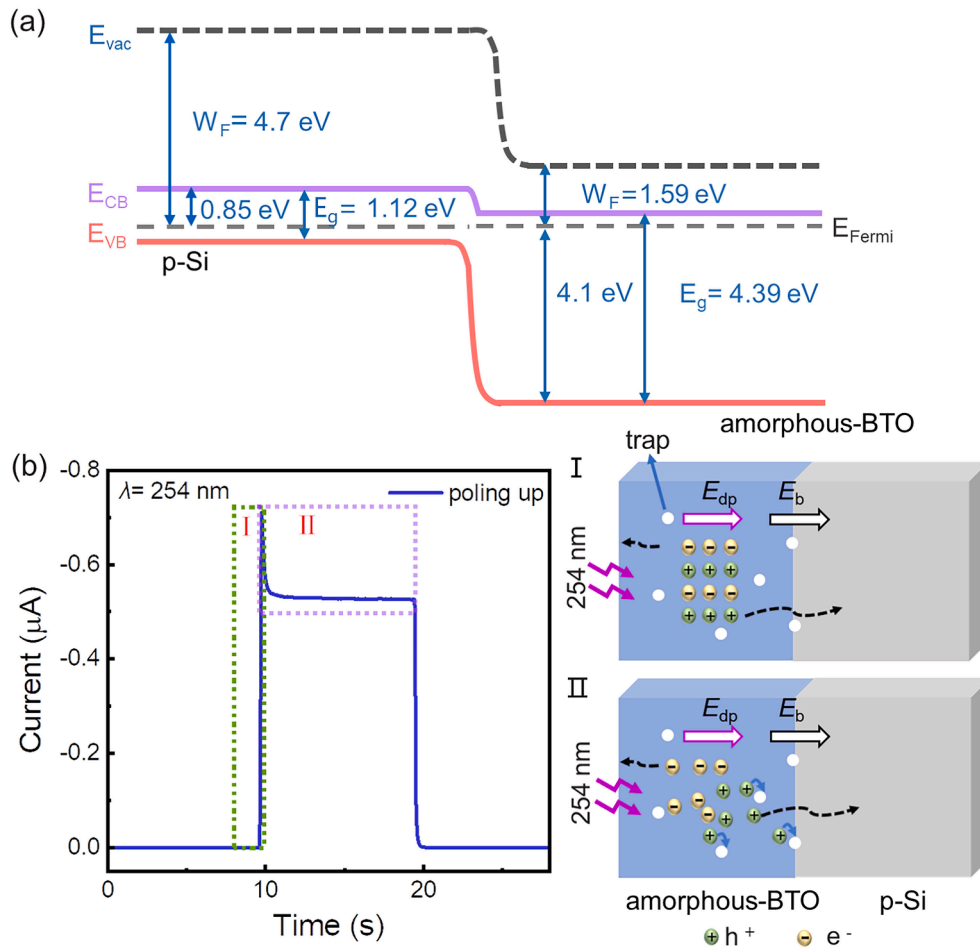
Fig. 6. (a) Energy band diagram of the equilibrium state of amorphous-BTO/p-Si junction in dark. (b) The schematic illustration of the carrier separation and trapping processes in amorphous-BTO/p-Si device.
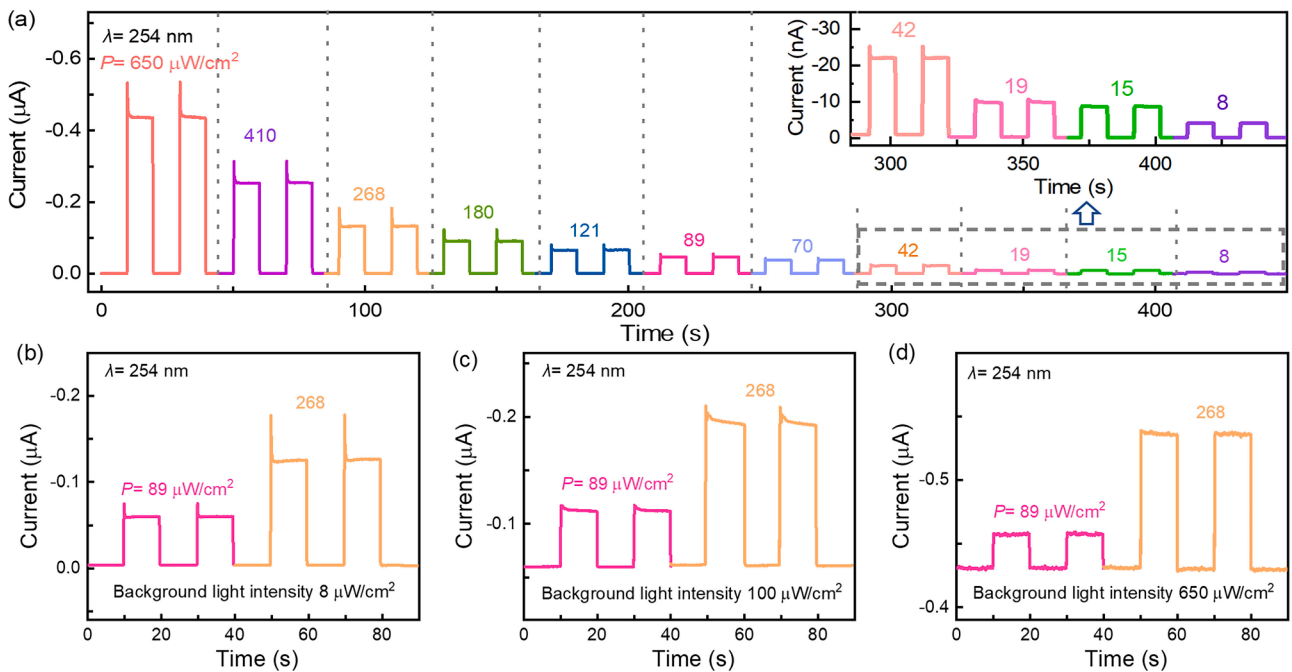

Fig. 7. (a) Photocurrent responses of the amorphous-BTO/p-Si device at 0 V bias under 254 nm light illumination with different intensities. (b)-(d) Influence of background light intensity on photocurrent dynamics.

transient spike current phenomenon can be illustrated in Fig. 6b. Previous reports suggest that the pyroelectric effect of ferroelectric materials can be used to explain the transient spike current phenomenon [21,23,38]. However, the pyroelectric current should strongly depend on temperature and undergo field-induced changes according to the polarization direction. In the present case, the amorphous-BTO/p-Si photodetector exhibits similar negative photocurrent spikes in polarized and unpoled states when the incident light is turned on, whereas no opposite spike can be observed when the incident light is turned off. Additionally, above the Curie point of BTO (120 °C), the transient spike can still be observed (Fig. 5a). Therefore, the pyroelectric effect cannot be regarded as the contributing factor to the photocurrent spike observed in the present study. Certain reports suggest that trap-assisted carrier recombination at the BTO interface may also lead to this transient spike current phenomenon [39,40]. When the 254 nm light is switched on, a large number of photogenerated carriers are generated in BTO and separated by the built-in electric field and the depolarization field. The resulting holes move to the p-Si side, while the electrons are transported to the BTO electrode (see Fig. 6). And thus, a prompt generation of photocurrent can be observed. Notably, such holes could be trapped or captured by the defects at the grain boundaries in the amorphous BTO and amorphous-BTO/p-Si interface. Such local accumulated trapped holes will recombine with free electrons via a defect-assisted carrier recombination process, resulting in a photocurrent decay. And a steady-state photocurrent can be obtained once the carrier generation and recombination rates attain a dynamic equilibrium [41,42].

To further study the transient response process, the photocurrent response curves of the device with and without background illumination were measured in the poling-up state at 25 °C. Fig. 7a demonstrates the time-dependent photocurrent under 254 nm light illumination with different intensities. At light intensities below 15 $\mu W/cm^2$, no photocurrent spikes are observed. This is because a limited number of photogenerated carriers are generated at such low light intensities, and only a few traps are filled; thus, the trap-assisted recombination rate is low. With increasing the light intensity above 19 $\mu W/cm^2$, more photogenerated carriers are generated and consequently, the trap-assisted recombination rate also increases, which in turn leads to a transient photocurrent spike. Further studies were conducted to investigate the effect of constant background illumination (254 nm) on the transient photocurrent behavior as shown in Fig. 7b-7d. When the background light intensity is set to 100 $\mu W/cm^2$, a part of the trap states will be filled by the carriers generated by the background light, but the recombination assisted by the unoccupied trap states still produces a slight overshoot after turning on the additional 254 nm light (Fig. 7c). Once the background light intensity increases to 650 $\mu W/cm^2$, the traps are almost fully filled, and thus no photocurrent spike can be observed (Fig. 7d). These results further confirm that the phenomenon of photocurrent transient spikes in the amorphous-BTO/p-Si heterojunction photodetector is related to the defect-assisted carrier recombination process at the amorphous-BTO/p-Si interface and amorphous BTO grain boundaries.

Table 1 shows a comparison of the responsivity and rising/fall time of the self-powered photodetector realized in this work with those of the reported devices based on BTO ferroelectric materials. The amorphous-BTO/p-Si device presented in this work exhibits superior self-powered photodetection performance. To the best of our knowledge, this device has the highest responsivity among the other reported self-powered BTO-based photodetectors due to the efficient combination of the depolarization field in BTO and the built-in electric field in the heterojunction. Additionally, the amorphous-BTO/p-Si photodetector exhibits almost the same self-powered photoresponse performance under different atmospheres (see Fig. S7). The present amorphous-BTO/p-Si device also benefits from a low-cost and large-area fabrication process.

Table 1

The representative works of the self-powered photodetectors based on the BTO.

Device structure	Wavelength (nm)	t_r/t_f (s)	Responsivity (A/W)	Ref.
ITO/BTO/Ag	405	0.4/1.6	$<3.5 \times 10^{-7}$	[10]
ITO/BTO/Ag	365	0.6/0.5	$\sim 10^{-7}$	[21]
Ag/BTO/Ag	365	0.56/13.44	$\sim 10^{-7}$	[22]
Au/BTO/Au	355	2×10^{-10}	1×10^{-5}	[24]
ITO/BTO/ITO	365	0.5/0.2	7.17×10^{-6}	[43]
Ag/BTO/Ag	365	0.5/23	6.1×10^{-8}	[44]
ITO/BTO/Ag	365	0.57/31.8	8.3×10^{-8}	[23]
ITO/BTO/Ag	405	0.88/1.06	–	[11]
ITO/BTO/ITO	405	-/-	$\sim 1 \times 10^{-6}$	[45]
amorphous-BTO/p-Si	UV(254)	4.5×10^{-4}/	1.4×10^{-2}	This work
	UV(365)	4.6×10^{-4}	2.7×10^{-2}	
	Visible(600)	6×10^{-5}/1.4 $\times 10^{-4}$	0.223	
		8×10^{-5}/1.4 $\times 10^{-4}$		

4. Conclusions

In summary, a high-performance self-powered UV–visible photodetector based on amorphous-BTO/p-Si has been designed and fabricated in the present work. Its photoresponse performance has been systematically investigated by tuning the polarization states of the amorphous BTO. Interestingly, the device in the poling-up state exhibited a significantly enhanced self-powered photodetection performance. This can be attributed to the efficient combination of the built-in electric field and the electric field caused by ferroelectric polarization. At 0 V bias, the responsivies of the device in the poling-up state reached up to 14, 27, and 223 mA/W at 254, 365, and 600 nm, respectively. To our knowledge, the responsivity achieved in this study is larger than any other reported BTO-based self-powered photodetectors. Moreover, a very fast response speed can be obtained with t_r/t_f of 450 µs/460 µs at 254 nm and 80 µs/140 µs at 600 nm. Besides, we have demonstrated that a transient peak in the photocurrent after turning on 254 nm illumination is associated with the defect-assistant recombination of photogenerated carriers at the amorphous-BTO/p-Si interface and amorphous BTO grain boundaries. This dependence was confirmed by investigating the influence of other parameters, including temperature, light power density, and background illumination. Our findings clarify the influence of the ferroelectric effect on the performance of ferroelectric semiconductor-based detectors and provide a novel strategy for developing high-performance self-powered photodetectors.

CRediT authorship contribution statement

Wushuang Han: Methodology, Investigation, Writing – original draft. **Kewei Liu:** Conceptualization, Validation, Supervision, Formal analysis, Visualization, Funding acquisition, Writing – review & editing. **Jialin Yang:** Supervision, Methodology, Data curation, Formal analysis. **Xing Chen:** Methodology, Formal analysis. **Qiu Ai:** Methodology, Formal analysis. **Yongxue Zhu:** Methodology, Formal analysis. **Zhen Cheng:** Methodology, Formal analysis. **Binghui Li:** Methodology. **Lei Liu:** Methodology. **Dezhen Shen:** Conceptualization, Resources.

Declaration of Competing Interest

The authors declare that they have no known competing financial interests or personal relationships that could have appeared to influence the work reported in this paper.

Data availability

Data will be made available on request.

Acknowledgment

Appendix A. Supplementary material

Supplementary data to this article can be found online at https://doi.org/10.1016/j.apsusc.2023.156371.

References

[1] X. Gong, M.H. Tong, Y.J. Xia, W.Z. Cai, J.S. Moon, Y. Cao, G. Yu, C.L. Shieh, B. Nilsson, A.J. Heeger, High-Detectivity Polymer Photodetectors with Spectral Response from 300 nm to 1450 nm, Science 325 (2009) 1665–1667, https://doi.org/10.1126/science.1176706.

[2] S.M. Hatch, J. Briscoe, S. Dunn, A Self-Powered ZnO-Nanorod/CuSCN UV Photodetector Exhibiting Rapid Response, Adv. Mater. 25 (2013) 867–871, https://doi.org/10.1002/adma.201204488.

[3] J. Yang, K. Liu, X. Chen, D. Shen, Recent advances in optoelectronic and microelectronic devices based on ultrawide-bandgap semiconductors, Progr. Quant. Electr. 83 (2022), 100397, https://doi.org/10.1016/j.pquantelec.2022.100397.

[4] D. Zhang, Y.H. Wang, Y. Yang, Design, Performance, and Application of Thermoelectric Nanogenerators, Small 15 (2019) 1805241, https://doi.org/10.1002/smll.201805241.

[5] H. Tang, D.L. Lu, Q.Q. Zhou, S.W. Luo, K. Huang, Z.Q. Li, X. Qi, J.X. Zhong, Self-powered and broadband flexible photodetectors based on vapor deposition grown antimony film, Appl. Surf. Sci. 571 (2022), 151335, https://doi.org/10.1016/j.apsusc.2021.151335.

[6] Q.Y. Zhang, J.P. Xu, M.H. Li, J. Chen, J.H. Xu, Q. Zheng, S.B. Shi, L.N. Kong, X.S. Zhang, L. Li, Applied Surface Science, High-performance self-powered ultraviolet photodetector based on BiOCl/TiO₂ heterojunctions: Carrier engineering of TiO₂, 592 (2022) 153350. https://dio.org/10.1016/j.apsusc.2022.153350.

[7] P.A. Shaikh, D. Shi, J.R.D. Retamal, A.D. Sheikh, M.A. Haque, C.F. Kang, H. He, O. M. Bakr, T. Wu, Schottky junctions on perovskite single crystals: light-modulated dielectric constant and self-biased photodetection, J. Mater. Chem. C. 4 (2016) 8304–8312, https://doi.org/10.1039/c6tc02828d.

[8] N. Deka, P. Chakraborty, D.C. Patra, S. Dhar, S.P. Mondal, Self-powered broadband photodetection using PbS decorated ZnO nanorods/reduced graphene oxide junction, Mater. Sci. Semicond. Process. 118 (2020), 105165, https://doi.org/10.1016/j.mssp.2020.105165.

[9] Y.M. Zhang, J. Chen, L.P. Zhu, Z.L. Wang, Self-Powered High-Responsivity Photodetectors Enhanced by the Pyro-Phototronic Effect Based on a BaTiO₃/GaN Heterojunction, Nano Lett. 21 (2021) 8808–8816, https://doi.org/10.1021/acs.nanolett.1c03171.

[10] N. Ma, K. Zhang, Y. Yang, Photovoltaic-Pyroelectric Coupled Effect Induced Electricity for Self-Powered Photodetector System, Adv. Mater. 29 (2017) 1703694, https://doi.org/10.1002/adma.201703694.

[11] K. Zhao, B.S. Ouyang, C.R. Bowen, Y. Yang, Enhanced photocurrent via ferro-pyro-phototronic effect in ferroelectric BaTiO3 materials for a self-powered flexible photodetector system, Nano Energy 77 (2020), 105152, https://doi.org/10.1016/j.nanoen.2020.105152.

[12] J. Chen, D. You, Y. Zhang, T. Zhang, C. Yao, Q. Zhang, M. Li, Y. Lu, Y. He, Highly Sensitive and Tunable Self-Powered UV Photodetectors Driven Jointly by p-n Junction and Ferroelectric Polarization, ACS Appl. Mater. Interf. 12 (2020) 53957–53965, https://doi.org/10.1021/acsami.0c15816.

[13] J. Shi, P. Zhao, X.D. Wang, Piezoelectric-Polarization-Enhanced Photovoltaic Performance in Depleted-Heterojunction Quantum-Dot Solar Cells, Adv. Mater. 25 (2013) 916–921, https://doi.org/10.1002/adma.201203021.

[14] W.B. Peng, Z.J. Pan, F.P. Li, Y.H. Cai, Y.N. He, Pyro-phototronic effect enhanced ZnO nanowire-based tri-layer heterojunction for visible light sensing and communication, Nano Energy 78 (2020), 105268, https://doi.org/10.1016/j.nanoen.2020.105268.

[15] Y. Zhang, X.Y. Zhao, J.X. Chen, S.Y. Li, W. Yang, X.S. Fang, Self-Polarized BaTiO₃ for Greatly Enhanced Performance of ZnO UV Photodetector by Regulating the Distribution of Electron Concentration, Adv. Funct. Mater. 30 (2020) 1907650, https://doi.org/10.1002/adfm.201907650.

[16] P.P. Biswas, S. Pal, V. Subramanian, P. Murugavel, Polarization driven self-biased and enhanced UV-visible photodetector characteristics of ferroelectric thin film, J. Phys. D-Appl. Phys. 53 (2020), 275302, https://doi.org/10.1088/1361-6463/ab83c3.

[17] I.H. Park, K.C. Kwon, Z.Y. Zhu, X. Wu, R.L. Li, Q.H. Xu, K.P. Loh, Self-Powered Photodetector Using Two-Dimensional Ferroelectric Dion-Jacobson Hybrid Perovskites, J. Am. Chem. Soc. 142 (2020) 18592–18598, https://doi.org/10.1021/jacs.0c08189.

[18] L. Chen, H.M. Li, Z. Wu, L.L. Feng, S.G. Yu, H.F. Zhang, J. Gao, Y.W. Mai, Y.M. Jia, Enhancement of pyroelectric catalysis of ferroelectric BaTiO₃ crystal: The action mechanism of electric poling, Ceram. Int. 46 (2020) 16763–16769, https://doi.org/10.1016/j.ceramint.2020.03.252.

[19] M. Acosta, N. Novak, V. Rojas, S. Patel, R. Vaish, J. Koruza, G.A. Rossetti, J. Rodel, BaTiO₃-based piezoelectrics: Fundamentals, current status, and perspectives, Appl. Phys. Rev. 4 (2017), 041305, https://doi.org/10.1063/1.4990046.

[20] T. Woldu, B. Raneesh, P. Sreekanth, M.V.R. Reddy, R. Philip, N. Kalarikkal, Size dependent nonlinear optical absorption in BaTiO₃ nanoparticles, Chem. Phys. Lett. 625 (2015) 58–63, https://doi.org/10.1016/j.cplett.2015.02.020.

[21] K. Song, N. Ma, Y.K. Mishra, R. Adelung, Y. Yang, Achieving Light-Induced Ultrahigh Pyroelectric Charge Density Toward Self-Powered UV Light Detection, Adv. Electr. Mater. 5 (2019) 1800413, https://doi.org/10.1002/aelm.201800413.

[22] N. Ma, Y. Yang, Boosted photocurrent in ferroelectric BaTiO₃ materials via two dimensional planar-structured contact configurations, Nano Energy 50 (2018) 417–424, https://doi.org/10.1016/j.nanoen.2018.05.069.

[23] Y. Ji, Y. Wang, Y. Yang, Photovoltaic–Pyroelectric–Piezoelectric Coupled Effect Induced Electricity for Self-Powered Coupled Sensing, Adv. Electr. Mater. 5 (2019) 1900195, https://doi.org/10.1002/aelm.201900195.

[24] J.K. Li, C. Ge, K.J. Jin, J.Y. Du, J.T. Yang, H.B. Lu, G.Z. Yang, Self-driven visible-blind photodetector based on ferroelectric perovskite oxides, Appl. Phys. Lett. 110 (2017), 142901, https://doi.org/10.1063/1.4979587.

[25] Y.P. Wang, X.F. Sun, T. Xian, G.R. Liu, H. Yang, Photocatalytic purification of simulated dye wastewater in different pH environments by using BaTiO₃/Bi₂WO₆ heterojunction photocatalysts, Opt. Mater. 113 (2021), 110853, https://doi.org/10.1016/j.optmat.2021.110853.

[26] K.V. Alex, A. Prabhakaran, A.R. Jayakrishnan, K. Kamakshi, J.P.B. Silva, K. C. Sekhar, Charge Coupling Enhanced Photocatalytic Activity of BaTiO₃/MoO₃ Heterostructures, ACS Appl. Mater. Interf. 11 (2019) 40114–40124, https://doi.org/10.1021/acsami.9b14919.

[27] T. Chen, J. Meng, S.Y. Wu, J.Y. Pei, Q.Y. Lin, X. Wei, J.X. Li, Z. Zhang, Room temperature synthesized BaTiO3 for photocatalytic hydrogen evolution, J. Alloy. Compd. 754 (2018) 184–189, https://doi.org/10.1016/j.jallcom.2018.04.300.

[28] T. Xian, H. Yang, L.J. Di, J.F. Dai, Enhanced photocatalytic activity of BaTiO₃@g-C₃N₄ for the degradation of methyl orange under simulated sunlight irradiation, J. Alloys Comp. 622 (2015) 1098–1104, https://doi.org/10.1016/j.jallcom.2014.11.051.

[29] W.T. Liu, S.T. Lakshmikumar, D.B. Knorr, T.M. Lu, I.G.A. Vanderleeden, Deposition of amorphous BaTiO₃ optical films at low-temperature, Appl. Phys. Lett. 63 (1993) 574–576, https://doi.org/10.1063/1.109981.

[30] X.M. Lu, J.S. Zhu, W.Y. Zhang, G.Q. Ma, Y.N. Wang, The energy gap of rf-sputtered BaTiO₃ films with different grain size, Thin Solid Films 274 (1996) 165–168, https://doi.org/10.1016/0040-6090(95)08000-7.

[31] H.Y. Tian, J. Choi, K. No, W.G. Luo, A.L. Ding, Effect of compositionally graded configuration on the optical properties of BaxSr1-xTiO3 thin films derived from a solution deposition route, Mater. Chem. Phys. 78 (2003) 138–143, https://doi.org/10.1016/s0254-0584(02)00223-7.

[32] C.-Y. Wei, S.-H. Kuo, Y.-M. Hung, W.-C. Huang, F. Adriyanto, Y.-H. Wang, High-Mobility Pentacene-Based Thin-Film Transistors With a Solution-Processed Barium Titanate Insulator, IEEE Electron Device Lett. 32 (2011) 90–92, https://doi.org/10.1109/led.2010.2084559.

[33] P.M. Razi, R.B. Gangineni, Compliance current and film thickness influence upon multi-level threshold resistive switching of amorphous BaTiO₃ (am-BTO) films in Ag/am-BTO/Ag cross point structures, Thin Solid Films 685 (2019) 59–65, https://doi.org/10.1016/j.tsf.2019.05.061.

[34] R.X. Wang, Q. Zhu, W.S. Wang, C.M. Fan, A.W. Xu, BaTiO₃-graphene nanocomposites: synthesis and visible light photocatalytic activity, New J. Chem. 39 (2015) 4407–4413, https://doi.org/10.1039/c4nj02272f.

[35] J.D. Mackenzie, Y.H. Xu, Ferroelectric materials by the sol-gel method, J. Sol-Gel Sci. Technol. 8 (1997) 673–679, https://doi.org/10.1023/a:1018336713418.

[36] S.S. Kumbhar, M.A. Mahadik, P.K. Chougule, V.S. Mohite, Y.M. Hunge, K. Y. Rajpure, A.V. Moholkar, C.H. Bhosale, Structural and electrical properties of barium titanate (BaTiO₃) thin films obtained by spray pyrolysis method, Mater. Sci, Poland. 33 (2015) 852–861, https://doi.org/10.1515/msp-2015-0107.

[37] C. Dubourdieu, J. Bruley, T.M. Arruda, A. Posadas, J. Jordan-Sweet, M.M. Frank, E. Cartier, D.J. Frank, S.V. Kalinin, A.A. Demkov, V. Narayanan, Switching of ferroelectric polarization in epitaxial BaTiO₃ films on silicon without a conducting bottom electrode, Nat. Nanotechnol. 8 (2013) 748–754, https://doi.org/10.1038/nnano.2013.192.

[38] L. Hu, S. Dalgleish, M.M. Matsushita, H. Yoshikawa, K. Awaga, Storage of an electric field for photocurrent generation in ferroelectric-functionalized organic devices, Nat. Commun. 5 (2014) 3279, https://doi.org/10.1038/ncomms4279.

[39] L.G. Hu, X. Liu, S. Dalgleish, M.M. Matsushita, H. Yoshikawa, K. Awaga, Organic optoelectronic interfaces with anomalous transient photocurrent, J. Mater. Chem. C. 3 (2015) 5122–5135, https://doi.org/10.1039/c5tc00414d.

[40] C.R. McNeill, I. Hwang, N.C. Greenham, Photocurrent transients in all-polymer solar cells: Trapping and detrapping effects, J. Appl. Phys. 106 (2009), 024507, https://doi.org/10.1063/1.3177337.

[41] H.X. Dong, Q.P. Liu, Y.H. He, Preparation of nanoporous BiVO₄/TiO₂/Ti film through electrodeposition for photoelectrochemical water splitting, Royal Soc. Open Sci. 5 (2018), 180728, https://doi.org/10.1098/rsos.180728.

[42] H.F. Zhang, C.W. Cheng, Three-Dimensional FTO/TiO₂/BiVO₄ Composite Inverse Opals Photoanode with Excellent Photoelectrochemical Performance, ACS Energy Lett. 2 (2017) 813–821, https://doi.org/10.1021/acsenergylett.7b00060.

[43] K. Zhao, B. Ouyang, Y. Yang, Enhancing Photocurrent of Radially Polarized Ferroelectric BaTiO3 Materials by Ferro-Pyro-Phototronic Effect, iScience. 3 (2018) 208–216, https://doi.org/10.1016/j.isci.2018.04.016.

[44] N. Ma, Y. Yang, Enhanced self-powered UV photoresponse of ferroelectric BaTiO$_3$ materials by pyroelectric effect, Nano Energy 40 (2017) 352–359, https://doi.org/10.1016/j.nanoen.2017.08.043.

[45] N. Ma, Y. Yang, Boosted photocurrent via cooling ferroelectric BaTiO3 materials for self-powered 405 nm light detection, Nano Energy 60 (2019) 95–102, https://doi.org/10.1016/j.nanoen.2019.03.036.